


Experimental comparison between an optical and an all-metal large bore engine

International J of Engine Research
2023, Vol. 24(3) 1223–1238
© IMechE 2022
Article reuse guidelines:
sagepub.com/journals-permissions
DOI: 10.1177/14680874221082794
journals.sagepub.com/home/ijer


Stephan Karmann¹, Stefan Eicheldinger², Maximilian Prager²,
Malte Jaensch² and Georg Wachtmeister¹

Abstract

Rising engine efficiency, increasingly stringent exhaust limits, and the use of synthetic and renewable fuels are all factors that demand a deeper knowledge of the combustion process. State-of-the-art investigations employ optical and laser-optical measurement techniques that rely on having optical access to the engine. In this paper, a new endoscopic system that provides full optical access to a high-speed large-bore engine is compared by thermodynamic experimentation to the equivalent all-metal engine. This comparison provides an insight into the altered combustion behavior resulting from modifying the engine to accommodate the optical elements. The successfully realized concept consists of two individually usable access points integrated in an engine with a bore of 170 mm and a stroke of 210 mm. The lateral endoscopic access is designed for full-load operating conditions and provides the best comparability to an all-metal engine. It is compared directly to the all-metal engine in the present investigations. Despite the changes in engine-out emissions from the optical engine, the experimental results display relatively equal combustion behavior in both setups. The lateral endoscopic access is then extended by adding a fisheye endoscope in place of one exhaust valve. This setup is compared to findings obtained with the endoscopic lateral access. The investigations reveal further deviations of the combustion process due to the more extensive modifications needed to fit the fisheye endoscope to the cylinder head. Nevertheless, the results display an overall good level of comparability of the combustion behaviors in these setups and, in turn, of the validity of further fundamental experiments based on the optical engine.

Keywords

Optical engine, large bore engine, port fuel injection, comparison of all-metal and optical engine, gas engine

Date received: 16 November 2021; accepted: 30 January 2022

Introduction

As the energy revolution continues, the use of renewable energies is expanding. In the EU, for example, the share of power consumption attributable to renewable energies increased from 8.5% in 2004 to 18% in 2018 (cf. Pressemitteilung Eurostat¹). In realizing a sustainable, cost-effective, and stable supply of energy in an industrialized and globalized world, the power to X process plays a key role in a sector-coupling approach. The power to X process stabilizes seasonal and regional fluctuations in residual loads by enabling the (long-term) storage of overproduced renewable energies in the form of renewable gaseous fuels such as hydrogen and methane and renewable synthetic liquid fuels such as OME. In existing infrastructures, synthetic methane or methane-hydrogen mixtures can replace fossil natural gas. In times of underproduction, renewably

generated chemical energy carriers can be used to stabilize the energy supply, for instance by reconverting them to electricity and heat in combined heat and power plants. For this purpose, stationary gas engines are known to be a reliable and efficient technology. To investigate the effects of new synthetic fuels on combustion, optical and laser-optical measurement methods are required, together with thermodynamic

¹Institute of Internal Combustion Engines, Technical University of Munich, Munchen, Bayern, Germany

²School of Engineering and Design, Technical University of Munich, Munchen, Germany

Corresponding author:

Stephan Karmann, Institute of Internal Combustion Engines, Technical University of Munich, Schragenhofstr. 31, Munchen, Bayern 80992, Germany.

Email: karmann@lvc.mw.tum.de

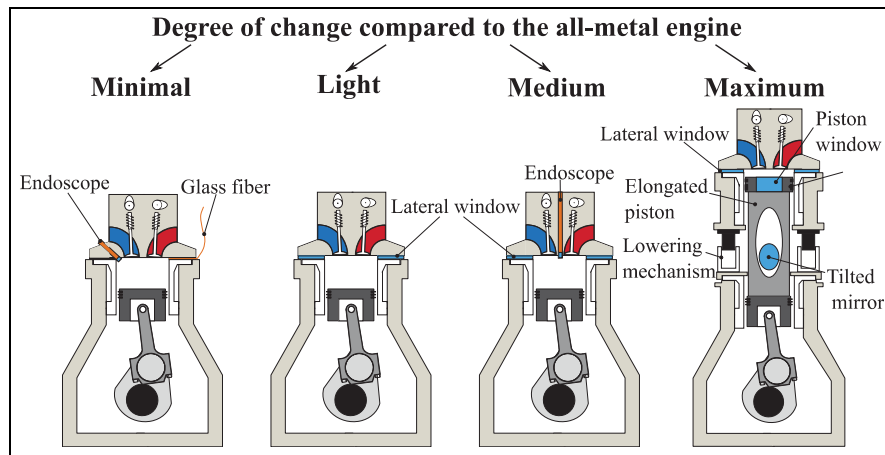


Figure 1. Degree of optical accessibility.

experiments. These techniques make it possible, for example, to assess the mixture composition during the gas exchange cycle; this has a direct effect on combustion, emission formation and combustion anomalies and, in turn, on engine efficiency. Combustion and the location of any anomalies that may occur (such as lube oil ignition, backfiring or knocking) can then be observed and understood. The basic prerequisite for these measurement techniques, which are already used widely in the passenger and truck vehicle displacement class to investigate synthetic fuels, for example (cf. Refs.²⁻¹¹), is that the engine permits optical access. Neither optical access nor the investigation of large bore engines are very common (cf. Refs.¹²⁻¹⁹). According to Karmann et al.,²⁰ Bensing,¹¹ there are four basic types of optical access, depending on the degree of change that this necessitates in relation to the all-metal engine (cf. Figure 1).

As the degree of optical accessibility and the modification requirements increase, the comparability of the optical setup with the all-metal engine decreases. This is mainly due to the introduction of glass components, resulting in changes to the heat transfer, modified engine components to accommodate the optical design, and, in some cases, the need to adapt the engine operation mode. Optical access with the maximum scope for modification is constructed according to the Bowditch principle²¹ and requires by definition:

- a modified crankshaft drive plus attendant changes to the tribological system of the piston and liner
- reduced engine speed due to increased inertia forces
- an increased proportion of glass components plus their temperature-sensitive mounts

Further adaptation of the operation to an often load-reduced skip fire operation mode is necessary. This approach is particularly common in the car and truck engine displacement class. Korb and Gleis present an application of this approach for a high-speed large-bore gas engine (cf. Refs.^{22,13,23,19}). The effects of the

maximum amount of change on engine behavior compared to the equivalent all-metal, for passenger-car-sized engines are shown in Colban et al.,²⁴ Kashdan et al.²⁵ and Kashdan and Thirouard²⁶ The engine-out emissions are particularly strongly affected. In order to overcome the disadvantages of the Bowditch approach in large bore engines, while also enabling maximum optical accessibility, an endoscopic method was developed for a high-speed large bore engine similar to that in Karmann et al.²⁷ This setup uses a fisheye endoscope to obtain a horizontal field of view inside the cylinder and a UV-optimized endoscope with an aperture angle of about 50° for a vertical field of view. This approach is in the medium change class according to Figure 1. The following describes the experimental comparison of the optical setup and all-metal engine that were performed to characterize the effects of the respective modifications on engine behavior.

Engine setup

Only a brief summary will be given here, as a detailed description of the three different engine setups can be found, for instance, in Eicheldinger et al.²⁸ for the all-metal engine and in Karmann et al.²⁹ for the optical setups. For simplification, the engine setups are denoted as 1 (all-metal engine), 2 (full-load optical setup) and 3 (full optical setup).

All-metal engine – setup 1

The all-metal engine is a single-cylinder research engine with a bore of 170 mm, a stroke of 210 mm, and a resulting displacement of 4.8 dm³. The engine can run on both gaseous and liquid fossil and renewable fuels in a variety of combustion processes, such as HPDF (high pressure dual fuel,^{13,30}) LPDF (low pressure dual fuel,³¹) or scavenged and unscavenged prechamber spark plugs.^{32,28} Figure 2 shows the setup consisting of the cylinder head, cylinder liner and liner housing. The setup uses as well as all further settings the same

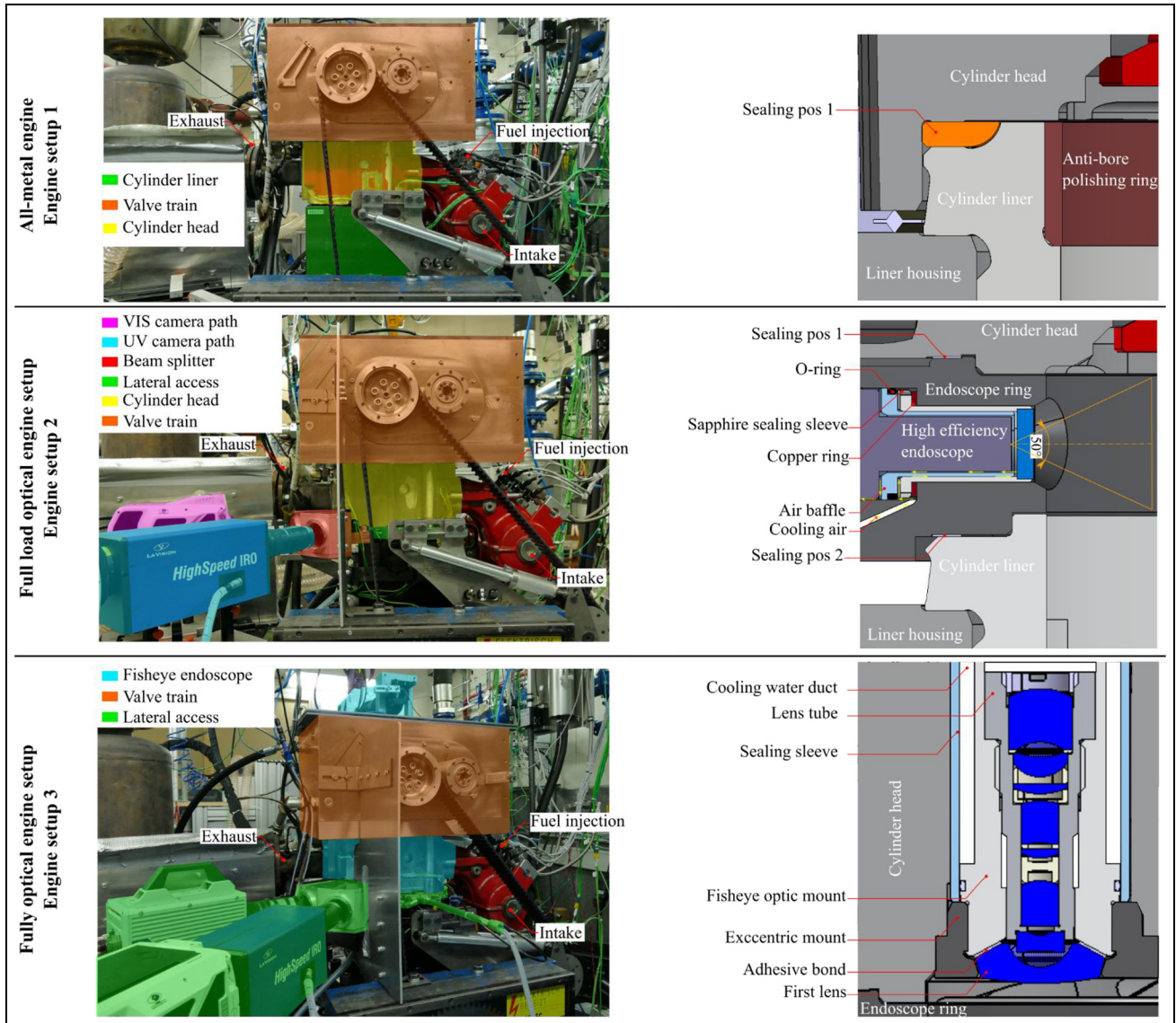


Figure 2. Overview of engine setups 1–3.

aluminum gas engine piston and piston rings. The parts are all commercially available series parts. The geometric compression ratio can be adjusted by inserting spacers between the liner housing and the base engine to modify the clearance height.

Full-load optical engine setup – setup 2

The optical setups are based on the design studies presented in Karmann et al.³³ and use the same testing rig infrastructure and base engine as Setup 1. The full-load optical setup consists of an endoscope ring integrated between the cylinder head and cylinder liner (cf. Figure 2). The endoscope ring is sealed with metal gaskets at Position 1 beneath the cylinder head and Position 2 on the liner. The setup uses adapted series parts, such as a slightly modified cylinder head and liner. To withstand continuous full-load operation conditions, water cooling is integrated into the

endoscope ring. The endoscope assembly further provides a self-developed air cooling system. Further, the sapphire sealing sleeve from FOS Meßtechnik GmbH can withstand 300 bar and 600°C and is modified to suit the air cooling, as shown in Figure 3. The endoscope ring offers three mounting positions for the LaVision high efficiency UV endoscope. The endoscope has a field angle of 25°. A beam splitter is used to simultaneously record both UV and natural-flame chemiluminescence in the visible spectral range, (cf. Figure 2).

In contrast to the all-metal engine, the full-load optical engine setup has a cooling circuit in the upper section of the liner where the endoscope ring is introduced, resulting in a relatively low cylinder wall temperature in this region. Due to the altered material, the endoscope ring (42CrMo4) has a lower heat conductivity than the original cylinder liner, which decreases the cooling effect by about 13%. The endoscope ring is fitted by

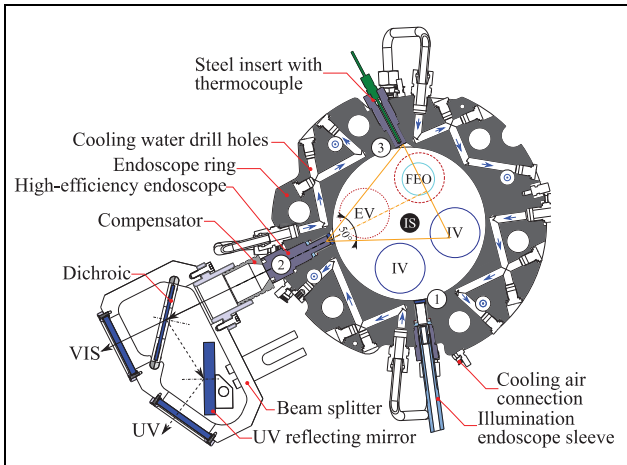


Figure 3. Horizontal sectional view of setup 2 and setup 3.

first removing the anti-bore polishing ring. As the overall run time of the engine during the tests was short, omitting this part is not critical. The presence of the endoscope ring increases the engine's dead volume by the second sealing height; this is also due to the recesses in the endoscope ring marking the endoscope positions. The dead volume arising from additional gaps due to the two sealing positions and the integration of the endoscope mounting holes increases to 1.75 times the dead volume of the all-metal engine (which equals an increase of 0.006l). To gain a constant compression ratio for the following experiments the clearance height was adjusted with the modification of the setup's liner housing and an adjustment of the spacers. The uncertainty of the geometric compression ratio amounts to ± 0.05 for the geometric compression ratio of 11.6 used in the following experiments, mainly due to manufacturing tolerances. Due to the high fire land of the piston with 25 mm, no further modifications are necessary to integrate the endoscope ring.

Full optical engine setup – setup 3

The full optical engine setup (cf. Figure 2) combines Setup 2 with a modified cylinder head capable of supporting a fisheye endoscope replacing one of the exhaust valves. This alters the gas exchange behavior due to the increased exhaust back pressure. The same additional dead volume as in Setup 2 arises in Setup 3 on account of the integration of the endoscope ring. As the exhaust valve is replaced by the fisheye endoscope and its mount, the additional dead volume causes a loss in the geometric compression ratio of about 0.7% at the compression ratio of 11.6. Due to non-optimized spacers for the adjustment of the compression ratio, as well as the uncertainty due to the manufacturing tolerances of the fisheye optic mount and the modifications at the cylinder head to fit the assembly, this small loss was acceptable and the compression ratio is assumed as equal. The first lens is made from quartz glass and is directly mounted in the combustion chamber. The lens

is glued precisely to its mount using a temperature-stable silicon-based adhesive capable of withstanding a 200°C continuous and 250°C peak temperature. To prevent the adhesive bond from overheating and failing, a strategy is required similar to those used in Bowditch-design engines (cf. Section 1). In Setup 3, skip fire engine operation is feasible for at least 150 fired cycles, thanks to the specially designed cooling system for the fisheye endoscope. The operating strategy of setup 3 is further detailed in section 3.3. The engine peak pressure has to be reduced to prevent the cylinder head from failure, as it is weakened by the modifications needed for mounting the optic. Simulations estimate that a minimum peak pressure of 180 bar can be endured, as shown in Karmann et al²⁹. The fisheye endoscope has a field angle of up to 180° and redirects the combustion's natural chemiluminescence via a 45° deflection mirror to the camera mounted outside the engine. The glass surface of the first lens diameter is 32 mm, which is only 3.5% of the bore area comparable less concerning the Bowditch principal with its large piston window.

Experimental setup and procedure

After the description of the different setup's designs the following summarizes briefly the testing rigs infrastructure equal for all three setups and the chosen experimental procedure.

Testing rig infrastructure

The test rig provides preconditioned and automated cooling water and oil supplies. Further, the test rig supplies pressure and temperature-controlled intake air at up to 9 bar. The air mass flow is measured using a rotary piston gas meter. The turbocharger is simulated by a controllable exhaust throttle, and the engine is connected to a coupled break, consisting of an induction machine and a dynamometer. The test rig provides both automated data acquisition and a control system. The fuel is natural gas from the municipal gas supply with a methane number of 90. The fuel mass flow is measured with a coriolis mass flow meter. The engine's exhaust pressure, intake pressure and combustion chamber pressure are indicated and logged by an automated measurement acquisition system. The recording rate of the fast measurement values is 0.1°CA. For combustion pressure recording the Kistler 6041B piezoelectric pressure transducer and 5011B charge amplifier are used. The measurement of the intake pressure is realized using a Kistler 4045A10 piezoresistive pressure transducer. The exhaust pressure is recorded with a Kistler piezoresistive pressure transducers 4075A10 in combination with a Kistler 7533B switching adapter. Both pressure transducers are connected to a corresponding Kistler charge amplifier 4603. To prove the plausibility of the recorded data, two slow pressure transducers in the intake and exhaust line of WIKA s10 type are used.

Setup and procedure

The full-load setup shown here is designed to be as close as possible in terms of its thermodynamic behavior to the all-metal engine with no lateral endoscopic access after a minimum of adjustments. The two setups are therefore compared directly. Further this comparison states the comparability of the findings described in Eicheldinger et al.³⁴ and Karmann et al.³⁵ with the all-metal engine.

The addition of the fisheye endoscope to the full-load setup can already be seen to have a significant effect, primarily on the gas exchange, and necessitates a reduction in the engine load (cf. Section 2). The two optical setups under reduced load are therefore compared and analyzed to determine the extent to which the combustion behavior is altered by the presence of the fisheye endoscope.

Water cooling for the fisheye optic was intended for the experiments, like it is described in Karmann et al.²⁹ Due to manufacturing issues that caused slight water leakage from the cooling duct into the lens setup, it had to be substituted by air cooling. Air cooling prevents contamination of the lens setting and still provides sufficient cooling to the lenses. Nevertheless, due to the reduced heat capacity and lower cooling capability of air, it was necessary to reduce the operation time of the fired engine. To compensate for this, the engine load was decreased further to a maximum peak pressure of 120 bar for the comparisons with the fisheye endoscope. Further, the engine's cooling water temperature was decreased by 5°C to extend the available measurement time. The nominal engine speed was reduced by 50% for both optical setups to prevent strong engine vibrations from affecting the cameras. Nevertheless, the designs without the cameras were still capable of achieving the nominal engine speed (cf. Karmann et al.²⁹).

Table 1 shows the data of the two setups in the following comparison.

Table 1. Overview of the experimental setup.

	Comparison 1: Engine setup 1 Engine setup 2	Comparison 2: Engine setup 2 Engine setup 3
ϵ	11.6 ± 0.4%	11.6 ± 0.7%
Engine Load	IMEP 21 bar	IMEP 16 bar
Injection pressure	12 bar	12 bar
Ignition	Unscavenged prechamber spark plug	
Engine speed for experiments	750 rpm	
Nominal engine speed	1500 rpm	
Sol	350°C a bFTDC	
Fuel	Natural gas	
Bore	170 mm	
Stroke	210 mm	
Conrod length	480 mm	

According to the detailed description given in Karmann et al.,²⁹ the exhaust valve lift was modified to account for the differences in gas exchange behavior. In contrast to the modification described in Karmann et al.,²⁹ the maximum lift of both valves is equalized. This is due to the use of a different cam profile in the experiment for Setups 1 and 2 than in the simulative investigations presented in Karmann et al.²⁹

The intake valve lift is the same in all setups. The valve lift of the exhaust valve is changed slightly in setup 3 to take advantage of the higher in-cylinder pressure when the exhaust valve is open and to enhance the exhaust gas mass flow.

The maximum lift is achieved almost simultaneously in all setups. Reducing the valve overlap causes the exhaust valve in Setup 3 to close 15°CA earlier than in both other setups. Figure 4 shows the measured valve lift curves for the exhaust and intake. The maximum exhaust valve lift is equal in all setups. 148 consecutive cycles are recorded for all setups and used for thermodynamic data processing. Setup 2 and 3 use 50 out of 148 cycles for image recording due to limited storage capacity of the camera setup. At each of the indicated measurement points the filtered combustion chamber pressure curves are corrected using a two-point polytropic offset correction. With a tuned GT-Power TPA (three pressure analysis) model the burning duration and heat release rate are derived, taking into account the wall heat losses calculated according to GT's so called WoschniGT approach.

The IMEP coefficient of variance, which is an indicator of combustion stability, is calculated by equation (1). Therefore, the corrected pressure traces used come directly from the data acquisition system of the test rig (cf. Chen et al.⁷).

$$CoV_{IMEP} = \frac{\sqrt{\frac{1}{N} \cdot \sum_{i=1}^N (IMEP_i - IMEP_m)^2}}{IMEP_m} \cdot 100 \% \quad (1)$$

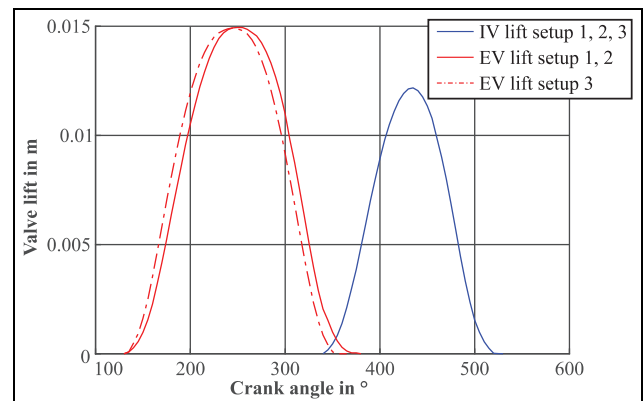


Figure 4. Valve lift (EV = Exhaust valve, IV = Intake valve).

Skip fire operation strategy

As already mentioned, only engine setup 3 uses a skip fire operation strategy to keep the temperature limits of the fisheye endoscope in certain simulative estimated (cf. Karmann et al.²⁹) bounds. Especially the temperature of the adhesive bond between the first lens of the optic and its mount limits the operation strategy and is therefore measured nearby for control. A similar approach was used in Karmann et al.²⁷ The start of the recording of thermodynamic values and the image capturing is controlled manually. Figure 5 shows the skip fire strategy for the measurement series of the CoC (center of combustion) variation for 10°C aFTDC on the left of the image and on the right of the image for 8°C aFTDC at an air-fuel equivalence ratio of 1.7. The CoC equals the 50% mass fraction burned. The image contains the temperature profile measured near the adhesive bond over the experiment time. The engine starts firing and reaches for the specified value of the CoC by online adjustment of the ignition timing to keep the CoC in the target with a range of $\pm 1.5^\circ\text{CA}$. The air mass needed for a specific air-fuel equivalence ratio was defined in preceding tests with a constant amount of fuel to reach a specific load.

The thermodynamic data recording starts when the fisheye endoscope reaches a temperature limit specified in preliminary tests and covers 148 fired cycles. The start temperature of the image recording is no fixed value, but actually depends on the actual air-fuel equivalence ratio, load and CoC resulting in a faster or slower heat up and thus higher or lower end temperature of the fisheye endoscope. Therefore, the start temperature is preliminarily derived for each investigated point meeting the boundary conditions of not reaching the automatic shut off temperature and providing a sufficient amount of fired cycles for a sufficient settling time to reach a stable combustion state. The image recording of 50 cycles starts with an offset of about 50 cycles to the thermodynamic data capturing to gain more settling time for the combustion. Figure 5 shows the automatic shut off temperature of 125°C.

The automatic measurement acquisition system provides two different recordings. One uses a slow 1Hz circle for continuous data logging. The fast one uses a resolution of 0.1°CA for the indication of the intake, exhaust and combustion chamber pressure. The continuous data logging freezes for about 4s shortly before the high resolution circuit finishes and uses the complete communication bandwidth between the real-time system and the control computer for storing the data. This results in Figure 5's visible logging freeze and the challenge not to pass the shut off temperature accidentally during this time without providing the actual control temperature, especially as this effect leads to a sudden temperature increase of about 5°C after finishing the data storing. A fired cycle sequence lasts on average for 74s respectively 462cycles.

After the fired cycles the fueling and ignition are shut off and the engine changes its operation from a fired to a motored one: the cool down cycles. During the unfired cycle sequence the engine cools down until reaching the start temperature of at most 85°C . Such a cool down duration was observed to last for up to 6minutes depending on the endoscope's end temperature.

Emission measurement under skip fire operation

Gleis¹³ investigated the response time of the same AVL FTIR as used for the following investigations under skip fire engine operation at a Bowditch type fully optically accessible HPDF engine. At least 70 fired cycles were needed before the measurement data recording reaches nearly constant emission levels. Nevertheless, as Gleis et al.¹³ uses a much more stable diesel combustion process and no other investigation from literature for a prechamber spark ignited optically engine was found, Figure 6 proofs the here achieved settling time sufficient for plausible emissions behavior. The settling time for the measurement of the emissions depicted in Figure 5 includes the duration from start of combustion detected as the first increase in the effective engine

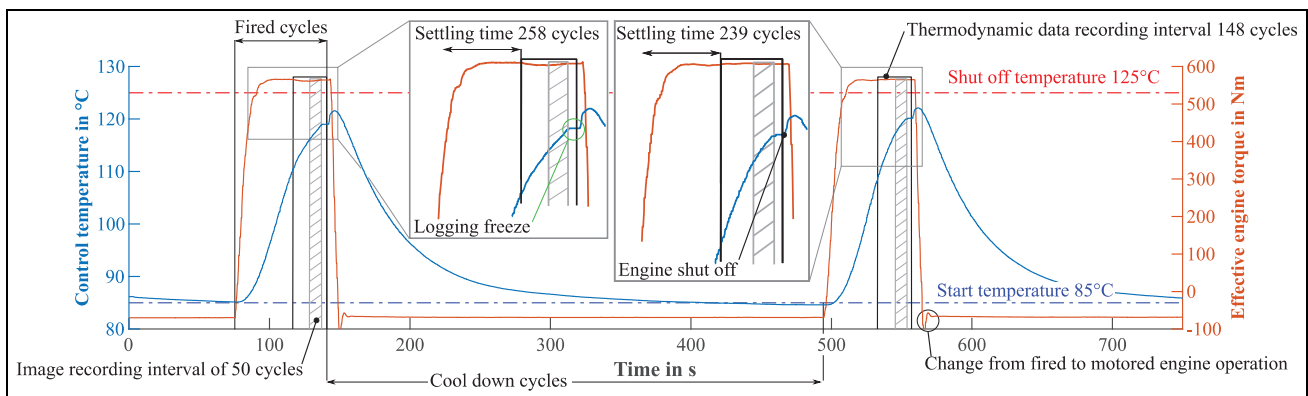


Figure 5. Skip fire operation strategy for air-fuel equivalence ratio 1.7 from left to right CoC variation for 10 and 8°CA aFTDC.

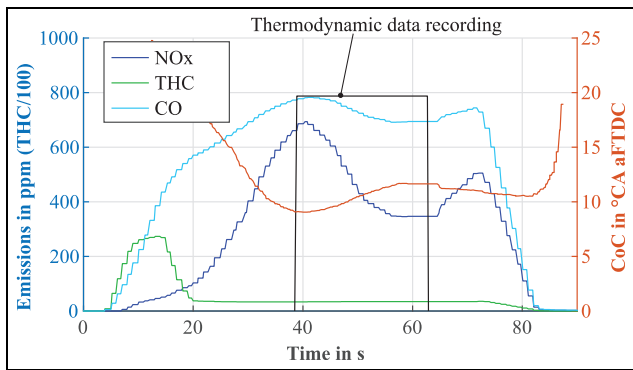


Figure 6. Emissions and CoC trace at air-fuel equivalence ratio 1.7 and CoC = 10°C aFTDC (THC emissions are scaled by a factor of 100).

torque until the start of the thermodynamic data recording. Further, Figure 6 shows exemplarily the trace of the online calculated CoC and measured emissions traces over time for data recording. Emissions are recorded and then averaged with a moving average of the last 10 values before getting logged with 1 HZ. The CoC is averaged over the last 148 working cycles and then logged with 1 HZ.

CO emissions show a maximum variation of 78.3 ppm during data logging, indicating that they are nearly constant throughout data recording. The THC emissions show even fewer deviations during the measurement interval. The increased variation of 314.2 ppm in NOx emissions during data logging is due to the high sensitivity of NOx formation to cyclic variations typical of spark ignited combustion processes. Since the emission traces of the remaining CoC variation show similar behavior in skip fire operation, the values can represent a clear trend in emission behavior over the conducted experiments and support the comparable behavior of engine Setup 3 with Setup 2. However, the comparison of absolute values, especially for NOx emissions is not recommended as long as no increase of stalling time is realized. To ensure that this variation in NOx emissions is not due to a fluctuating air to fuel equivalence ratio, Figure 7 examines air mass flow and fuel mass flow at a CoC of 10°C aFTDC in skip fire operation.

The target gas mass flow of 8.44 kg/h is reached with a peak deviation of 0.35% during the recording period. The target air mass flow of 247.5 kg/h is achieved with a maximum deviation of 1.7% in the recording period. If the measurement uncertainty of the air mass flow meter and the coriolis gas flow sensor are also taken into account, the deviation of the air to fuel equivalence ratio can be specified. The target value of 1.7 can be reached within a deviation of ± 0.027 respectively 1.58% during recording. This is sufficiently accurate for the investigations and for stable combustion.

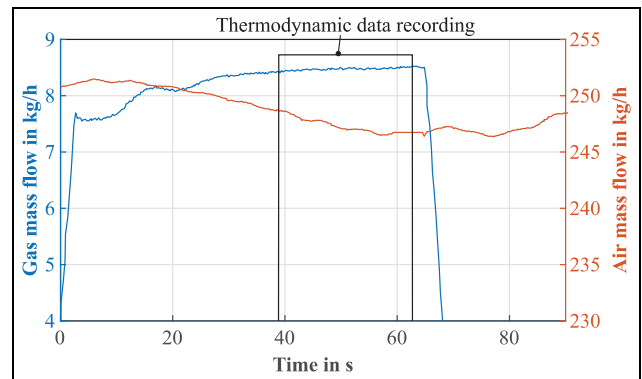


Figure 7. Gas and air mass traces at air-fuel equivalence ratio 1.7 and CoC = 10°C aFTDC.

Experimental comparison between the all-metal engine and the full-load optical engine setup: Comparison I

To compare the all-metal engine with the full-load optical engine setup, an air-fuel equivalence ratio and CoC (center of combustion) which equals the MFB 50 (50% mass fraction burned) variation map is considered at a constant load of up to 21 bar IMEP (indicated mean effective pressure). The air-fuel equivalence ratio variation is evaluated in steps of 0.05 from 1.5 to 1.85. The uncertainty of the lambda calculation is 0.23% resulting from the accuracy of the measurement devices. The CoC is investigated at $8^{\pm 1}$, $10^{\pm 1.5}$, $15^{\pm 1.5}$, $20^{\pm 1.5}$ and $25^{\pm 1.5}$ °CA aFTDC. The specified uncertainties are due to the engine control tolerances. Regarding the theoretical thermodynamic optimum, the following evaluation focuses on the CoC at 8°C aFTDC. The measurement data are evaluated for combustion and emission behavior.

Combustion pressure

Figure 8 shows the recorded combustion pressure trace of Setups 1 and 2. Between compression from 80°C aFTDC to FTDC at 0°C aFTDC, there is only a slight deviation in the pressure trace, resulting from different wall heat losses in the two setups. The maximum combustion pressure only deviates by 0.3 bar. The shift between the traces is due to a delay of 4.25°C aFTDC in the ignition timing of engine setup 1 due to a difference in the burn duration shown in Figure 9(a). During the expansion and exhaust stroke, the pressure traces are almost equal again.

Combustion behavior

Due to the difference in the ignition timing needed to reach the same CoC of the thermodynamic optimum at

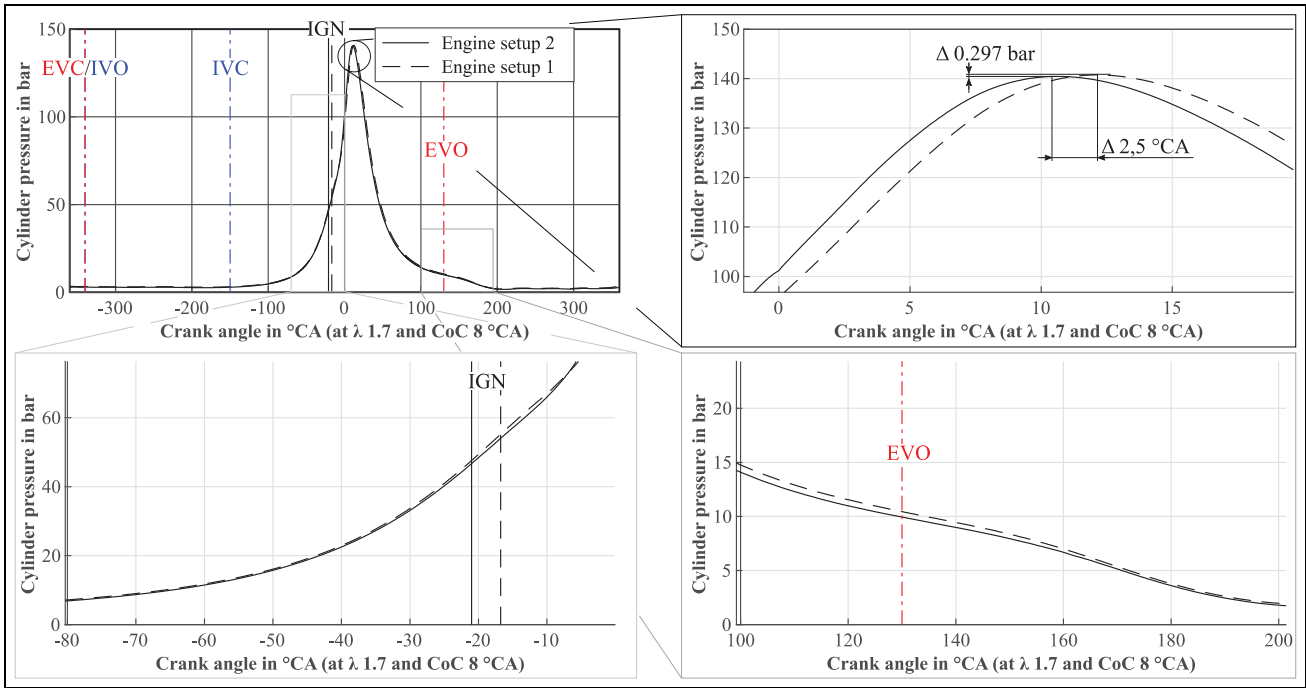


Figure 8. Combustion pressure trace at an air-fuel equivalence ratio of 1.7 and CoC 8 °CA aFTDC.

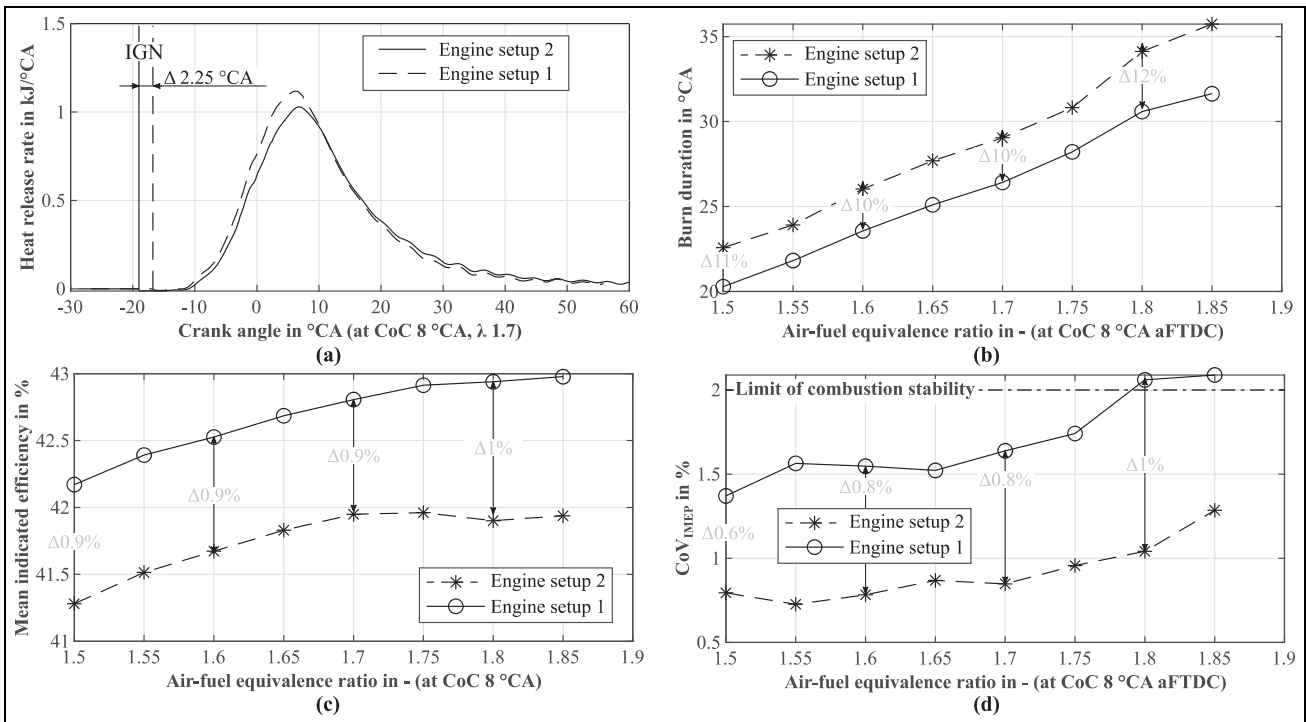


Figure 9. Combustion behavior in Comparison I: (a) heat release, (b) burn duration MFB 10–90, (c) mean indicated efficiency, and (d) CoV_{IMEP} .

8 °CA, the heat release rate in Setup 1 is before the trace of engine setup 2 (cf. Figure 9(a)). This is also due to an apparent increased ignition delay in Setup 2. The maximum heat release is lower for Setup 2 and has a slightly slower trace, hinting at a decrease in combustion temperature and a possible different air-fuel distribution in

the combustion chamber. The peak difference in the two traces is due to a slight increase in the wall heat loss and delayed combustion for Setup 2. The burn duration from MFB 10 to MFB 90 shows an almost constant offset of about 3 °CA observed over the air-fuel equivalence ratio variation (cf. Figure 9(b)). This may be due

to cooler combustion chamber walls and increased quenching in Setup 2. The lower wall temperature is due to endoscope ring cooling, whereas engine setup 1 does not provide any cooling duct in the vicinity of the anti-bore polishing ring. The shorter burning duration in Setup 1 and the lower wall heat loss and dead volume lead to an increased indicated mean efficiency of at least 1% compared to engine setup 2, as shown in Figure 9(c). The variance coefficient of indicated mean effective pressure shows more unstable combustion in Setup 1, with differences of up to 1%. As the optimal thermodynamic center of combustion of 8°CA aFTDC is attained, ignition conditions such as pressure and temperature are at their optimum compared to later CoCs. The assumption made here is that due to the cooler combustion chamber a reduced laminar burning velocity creates less intense combustion concerning the heat release and pressure rise rate in Setup 2 than in Setup 1. Uneven fuel distribution in the fresh charge leads to uneven flame propagation, which is reflected as a pressure variation in the cycles. This has a negative effect on the uniformity of combustion from cycle to cycle. An increased level of cylinder charge temperature tends to amplify the inhomogeneous flame spreading. This effect affects Setup 2 less than setup 1 due to the cooler combustion chamber, which could cause the more stable combustion shown in Figure 9. A further detailed investigation is necessary to proof the extent of this influence. Furthermore, it can be assumed that the design adjustments lead to a change in the cylinder liner tension, which can increase the lube oil ingress via the piston ring pack. The spread of oil contributes to combustion stability as an additional, spatially distributed ignition source. Setup 1 in particular exceeds the limit of CoV_{IMEP} proposed in Park et al.³⁶ Moreover, the combustion stability decreases as the air-fuel equivalence ratio increases due to the reduction in laminar flame speed and the deterioration in the ignition conditions as the combustion becomes leaner.

Engine-out emissions

Engine-out emissions are measured with an AVL Sesam FTIR, and are shown in Figure 10. CO

emissions increase continuously as the air-fuel equivalence ratio varies and display a colder after-burn phase in Setup 2 (cf. Figure 10(a)) than in Setup 1, which prevents the temperature-dependent oxidation of CO. This is because the decreased wall temperatures facilitate heat transfer into the wall, which reduces the burnt gas temperature and thus prevents further oxidation of CO. The decrease in CO at higher air-fuel equivalence ratios is due to the lower amount of oxidized fuel that can be discerned as the THC emissions increase, owing to the deteriorated lean combustion conditions. The mean increase in CO emissions from Setup 1 to Setup 2 is 32%.

The slightly lower mean combustion temperature does not decrease the NO_x emissions shown in Figure 10(b). With only slightly lower thermal NO_x formation in the flame front, both setups show almost equal NO_x emissions. This indicates similar peak combustion temperatures and a different after burn phase, influenced in particular by the wall temperature of the combustion chamber. The high level of NO_x emissions is due to the formation factors of time and temperature, as the reduced nominal engine speed doubles the formation time, and therefore, the NO_x emissions of the engine at nominal speed are lower.

THC emissions are also higher in Setup 2 (cf. Figure 10). This is due to the slightly lower combustion temperature, resulting either in a longer burn duration (cf. Figure 9(a)), with a reduced laminar flame speed and increased quenching distance. The longer quenching distance is also due to the lower combustion chamber wall temperature. As the cold wall reduces the radical formation due to the increased heat transfer from the flame front to the wall, the combustion propagation deteriorates. Therefore, the near-wall regions, in particular contain unburnt hydrocarbons, especially methane. Furthermore, the full-load optical engine setup has an increased dead volume because of the two sealing positions, instead of only one in engine setup 1. Additionally, the gaps around the endoscope mounting positions are not covered by the flame and therefore hold unburnt gas. All in all, the dead volume of Setup 2 in contrast to Setup 1 is increased 1.75 times resulting in 0.006l (cf. section 2.2). Taking this into account, a

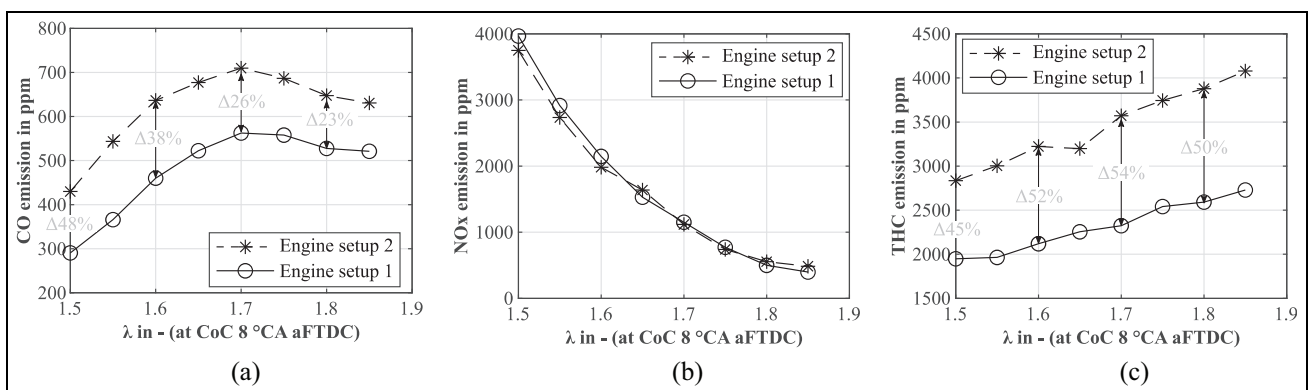


Figure 10. Emissions in comparison I: (a) CO emission, (b) NO_x emission, and (c) CO emission.

mean increase of 49% in THC emissions seems plausible as Korb³² already mentions the dead volume reduction as a possible cause for a decrease in THC emissions of up to 30%. Simulative 3D-CFD investigations of the influence of dead volume and flame wall quenching on THC emissions in Kuppa et al.³⁷ point to a greater influence of the dead volume than the quenching.

Combustion chamber temperature

The cylinder head temperature is measured near the flame deck at four different locations between the valves in 4 mm ± 0.1 mm depth from the flame deck. The circumferential distribution is shown in Figure 11(a). Position 4 indicates the maximum cylinder head temperature, being located between the two exhaust valves. The cylinder head temperature shown in Figure 11(a) is almost equal in both engine setups, except at Position 4. The temperature difference at Position 4 is a result of the receded measurement position in Setup 2. This receded position is due to the equal raw parts strategy used for Setup 2 and 3. The two setups have the same basic modifications at the cylinder head for integrating the endoscope ring and the modifications for thermodynamic measurements, for example, the addition of thermocouples and a cylinder pressure sensor. Setup 3 requires further machining to integrate the fisheye endoscope, especially at the region of the exhaust valve. So the position of Thermocouple 4 is altered. The almost equal temperature at the other measurement positions

in the cylinder head is due to the cylinder head cooling duct being unmodified. Further, as the same amount of fuel energy is introduced, the same amount of heat is released, disregarding slight differences arising from the slightly altered combustion.

Setup 1 contains three thermocouples on the pressure side and three on the counter pressure side of the liner in a depth of 0.3 mm ± 0.1 mm. The nearest ones to the cylinder head (Positions 1 and 2 in Figure 11(b)) offer the best comparability to thermocouples in the endoscope ring. Therefore these are taken as input for the average value for the comparison of the two setups shown in Figure 11(b).

The endoscope ring contains seven thermocouples (not shown in Figure 11(b)). Three thermocouples can be positioned in the screw in positions (cf. Figure 3) using steel inserts with a 3 mm ± 0.1 mm distance from the combustion chamber wall surface to the tip of the thermocouple. Position A in Figure 11(b) has a steel insert fitted with a thermocouple. Three more monitor the temperature near these positions. The seventh thermocouple (Position B in Figure 11(b)) measures the wall temperature of the endoscope ring in the inlet half of the combustion chamber with a distance of 1.8 mm ± 0.1 mm from the thermocouple tip to the inner chamber surface.

Since the measurement positions of the two engine setups do not exactly match, the positions A and B shown in Figure 11(b) have been chosen, as they are the closest available. To simplify the comparison, the values are taken as a mean value. Hence, Setup 2 results in

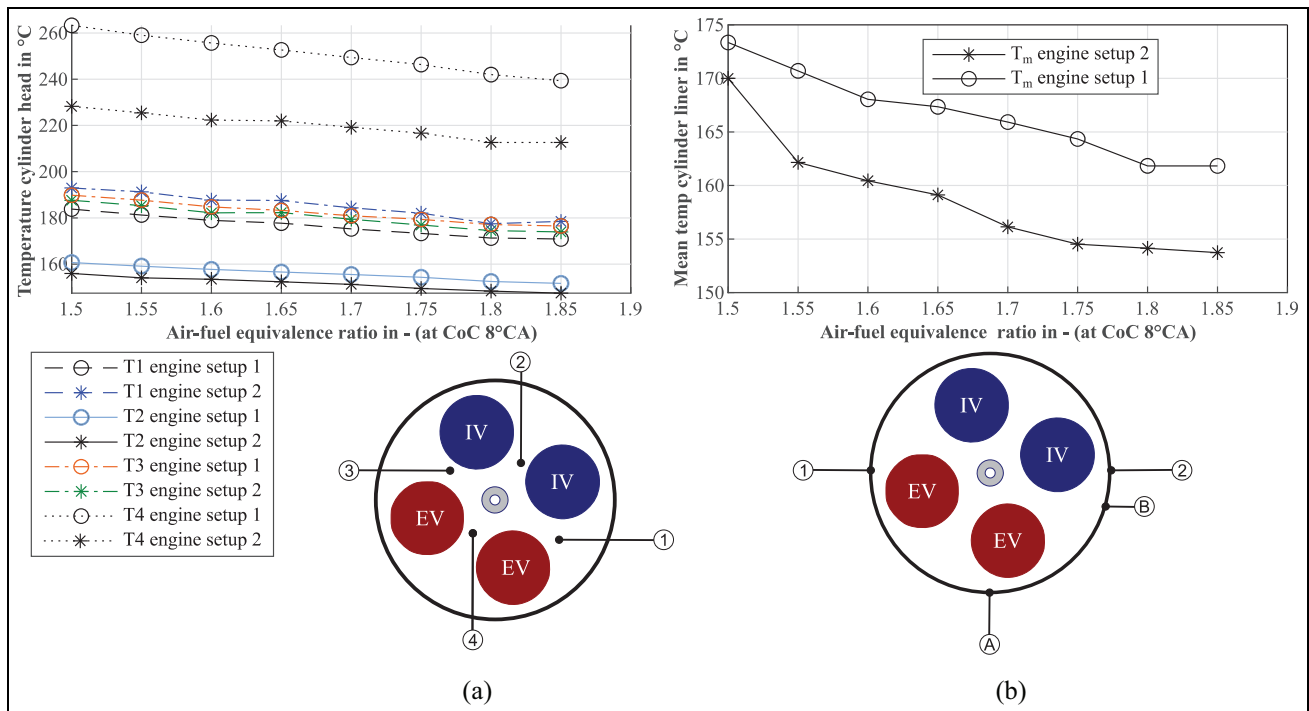


Figure 11. Wall temperature in Comparison I: (a) cylinder head temperature and (b) mean cylinder wall temperatures (1–2 Setup 1) A–B (Setup 2).

a lower mean temperature of about 8°C . The temperature reduction resulting from endoscope ring cooling supports the explanation of the combustion behavior.

Experimental comparison between the full-load optical and fully optical engine setups: Comparison 2

To compare the full-load optical engine setup with the full optical engine setup, a CoC variation at a constant load of 16 bar IMEP and a constant excess air ratio of 1.7 is analyzed, as no complete variation map of the air-fuel equivalence ratio and CoC is available. Engine setup 3 runs in skip fire operation mode detailed in section 3.3, whereas Setup 2 runs continuously in normal steady state operation. This comparison can be used to evaluate the comparability of Setup 3 versus Setup 2 and the suitability of skip fire operation. The following section presents the measurement data for combustion and emissions and the observed behavior.

Combustion pressure

Figure 12 evaluates the combustion pressure trace at CoC 8°CA aFTDC for an air-fuel equivalence ratio of 1.7. Due to the relatively small difference in the ignition timing of 0.75°CA , the pressure traces show no shift and are almost equivalent. The compression phase also matches quite well, resulting in a comparable combustion process for both setups. Nevertheless, the maximum combustion pressure of the full optical engine is 3.3 bar lower than in the full-load optical engine setup,

resulting in a 3% deviation. This could be due to a slight deviation in the compression ratio as well as less intense combustion due to incomplete gas exchange and lower in-cylinder combustion temperatures. The lower gas exchange efficiency is related to the increased exhaust backpressure, as one exhaust valve is replaced by the fisheye endoscope, as described in Section 2. This behavior can be seen in Figure 12, as the combustion pressure after EVO is higher for Setup 3 than for Setup 2, even though the exhaust flap for simulating a turbocharger is fully open to compensate for this elevated pressure. In contrast, Setup 2 uses a simulated exhaust flap with a turbo charger efficiency of 75%.

Combustion behavior

The cumulative heat release rate shown in Figure 13(a) points to almost equal combustion behavior in both setups, as the start and ascent behaviors are quite similar. This can also be attributed to the very similar ignition timing with a difference of 0.75°CA .

The lower maximum of the heat release rate in Setup 3 supports the assumption that the combustion is less intense regarding a decreased laminar burning velocity. This has several reasons. One main effect is the lower combustion chamber wall temperature, which results in an increased heat loss toward the wall and therefore reduces the charge temperature at the beginning and during the combustion. Further, this effect supports a delayed ignition and contributes to a decreased heat release rate.

The modifications of the valve lift in Setup 3 decrease the effect of the remaining amount of residual

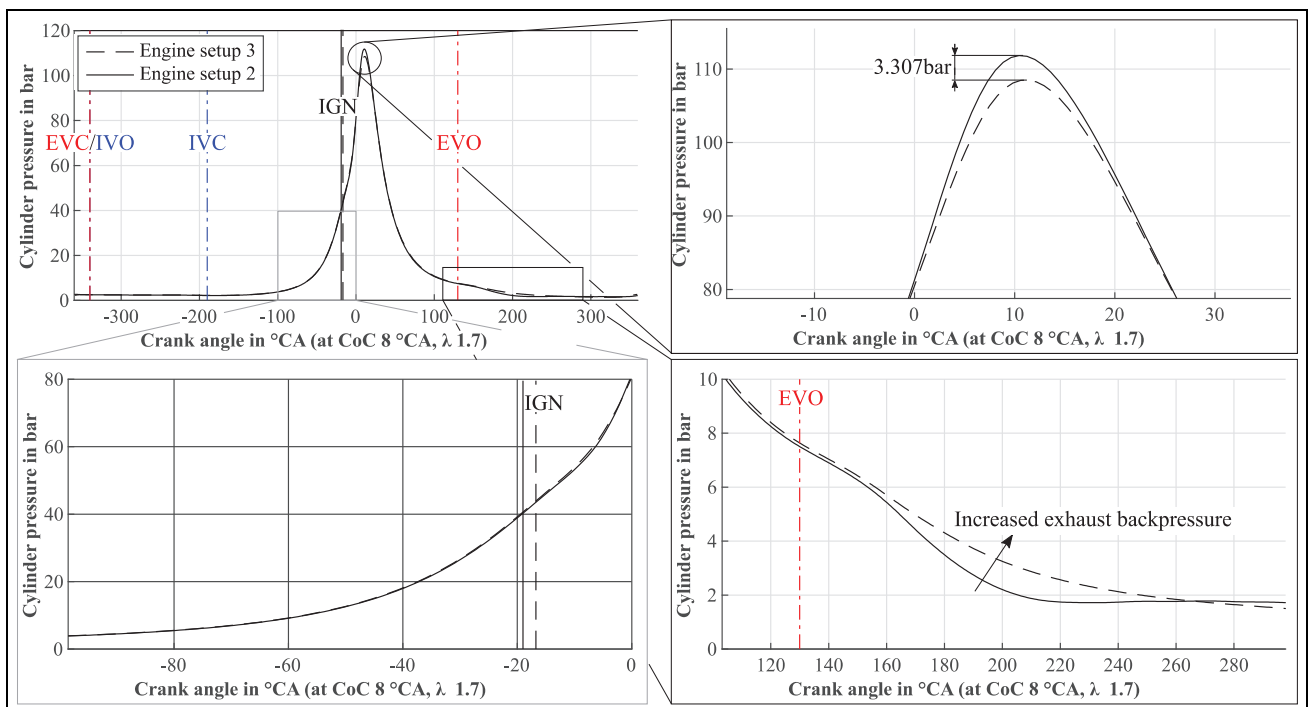


Figure 12. Combustion pressure at CoC 8°CA , air-fuel equivalence ratio 1.7 for comparison 2.

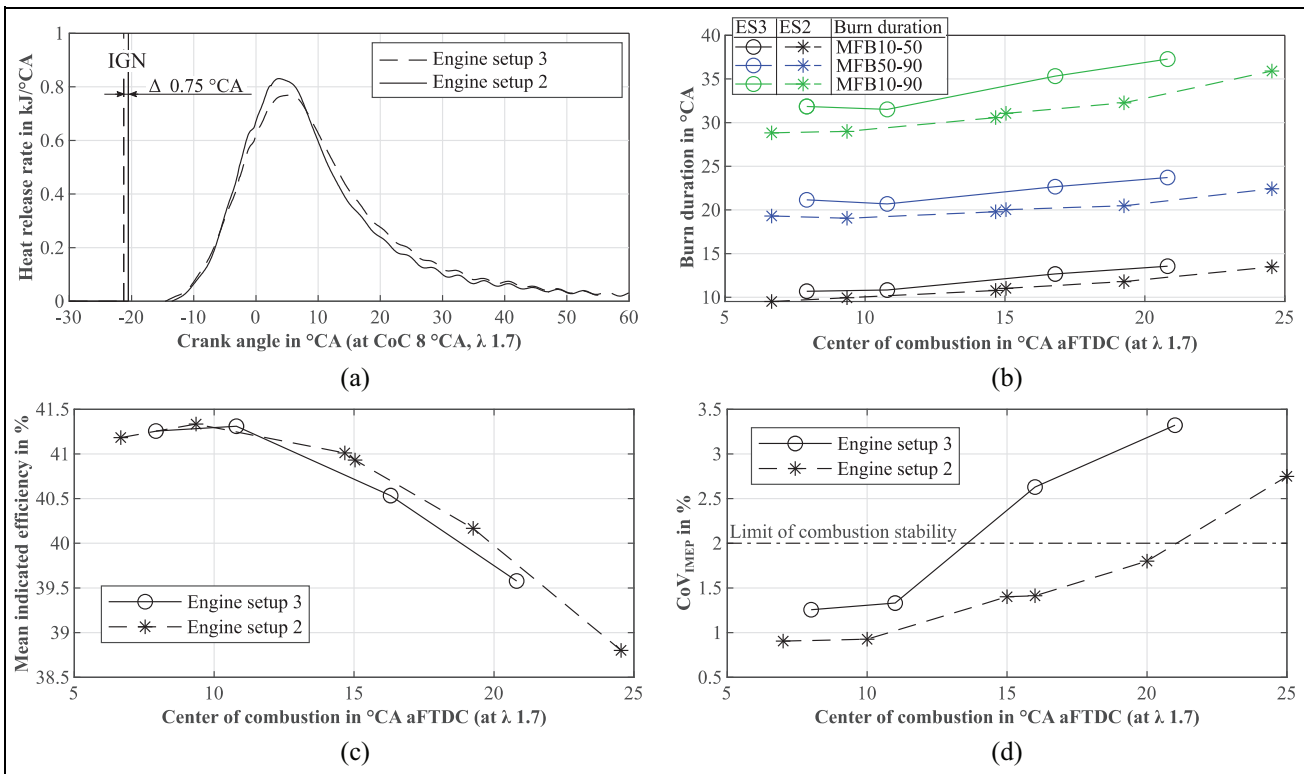


Figure 13. Combustion behavior in Comparison 2: (a) heat release, (b) burn duration (ES2 = engine setup 2, ES3 = engine setup 3), (c) mean indicated efficiency, and (d) CoV_{IMEP}.

gas as only a small deviation of the ignition timing and a close matching heat release are observable. Further, the GT-Power model used for the TPA calculates a mean increase of the residual gas mass percent at combustion start over the experiments of 1.1%. Therefore, the slightly increased residual gas mass contributes to the delayed combustion.

Figure 13(b) shows the burn duration for the main combustion from MFB10-50, for the late combustion from MFB50-90 and the complete combustion duration from MFB10-90 for both engine Setups 2 and 3. For the main combustion, engine Setup 3 has a mean deviation of 1.4°CA to Setup 2. This hints that the main combustion matches quite well comparing both Setups providing almost similar combustion conditions. The late combustion duration shows a mean difference of 2.3°CA, which is 63% more than in the main stage of the combustion. This hints at a delayed combustion due to a decrease in the laminar burn velocity. As the combustion conditions deteriorate in this stage of the combustion, the reduction of the laminar burn velocity in engine Setup 3 further suffers from increased wall heat loss.

Nevertheless, the combustion durations are comparable, especially with CoCs near the thermodynamic optimum, supporting the combustion with good ignition and flame propagation conditions. With late CoCs the combustion conditions deteriorate resulting in a higher burn duration for each setup and therefore also in an increased difference because of the accumulation

of deviation over time. For the complete combustion duration, the mean difference over all experiments results in 12%.

The mean indicated efficiency is almost equal in both setups but deteriorates at late CoCs further in Setup 3 (cf. Figure 13(c)). For early CoCs, the combustion and ignition conditions are well matched and hardly any deviation is discernible even with the deterioration of the combustion in Setup 3 relative to Setup 2. This relative equality is also due to the higher combustion temperature and shorter burning duration at early CoCs of Setup 2, resulting in a shorter duration for wall heat loss and more complete combustion. Setup 3 on the other hand shows an efficiency drop due to the increased burn duration for late CoCs owing to the deteriorated combustion and ignition conditions. Since a late CoC results in delayed and more incomplete combustion, the efficiency decreases. This is especially true in Setup 3, as the quenching distance increases due to the colder combustion chamber wall and lower combustion temperature, resulting in even more incomplete combustion, also indicated by the increased amount of THC in the exhaust gas (cf. Figure 14(c)).

The combustion stability of Setup 3 undergoes deterioration in all investigations compared to the other setup, as only this setup operates in skip fire engine mode, which does not entirely reach the same stationary and stable engine operating conditions as in Setup 2. Figure 13(d) illustrates this behavior. Considering the

early center of combustion, the combustion destabilizes as the ignition conditions deteriorate. This does not get better as the engine continues to heat up and offers no stable ignition conditions. Nevertheless, both engine setups display the expected combustion behavior over the investigated CoC sweep at an air-fuel equivalence ratio of 1.7, which is an effect of the modifications. As the CoV_{IMEP} is derived directly from the measurements without consideration of the TPA model, the corresponding CoC points are also derived directly from the measurements, resulting in a slight offset compared to the CoC values derived from the TPA model.

Engine-out emissions

With respect to section 3.3, the emissions of CO and THC show a promising stable emission behavior, whereas the NO_x emissions seem more unstable. Therefore, the findings especially concerning the NO_x emissions can only be interpreted as tendencies not absolute values with the possible contributing effects explained for a profound overview.

With regard to the engine-out emission behavior in Comparison 2, both setups show almost the same level of CO emissions (cf. Figure 14(a)).

For late CoCs, the lower peak combustion temperature tends to increase CO emissions, but this effect is outweighed by the prolonged combustion, which leads to prolonged oxidation also in the exhaust gas. Finally, both setups have roughly equal THC emissions, as illustrated in Figure 14(c). Although Setup 3 operates in skip fire mode, the THC emissions are about 7% lower than in Setup 2. The increased amount of residual gas keeps unburnt fuel in the cylinder and increases the average gas temperature over the working cycle. Both promote the oxidation of THC.

The fewer NO_x emissions shown in Figure 14(b) for Setup 3 is due to the lower peak combustion temperature resulting from the slightly increased recirculation of the in-engine exhaust gas and the skip fire operation and increased cooling. However, at the

same time, the increased residual gas acts as a thermal insulator during the after burning phase and thus prevents wall heat loss, resulting in a higher post-oxidation temperature.

Combustion chamber temperature

The effects of the 5°C reduction in cooling water temperature and the skip fire engine operation are reflected in the temperature profiles of the cylinder head and the cylinder liner wall, which are shown in Figure 15.

The temperature measurement positions in the cylinder head are equal in both setups lying $4\text{ mm} \pm 0.1\text{ mm}$ below the flame deck. The measurement positions in the endoscope ring are placed in a steel insert for positions A and C with a material coverage depth of $3\text{ mm} \pm 0.1\text{ mm}$. Position B is similar to the one used for comparison 1 and is positioned in a depth of $1.8\text{ mm} \pm 0.1\text{ mm}$. Position D is near the endoscope and has a distance of $7\text{ mm} \pm 0.1\text{ mm}$ to the combustion chamber surface. The values shown are mean temperatures derived from all measurement positions in the cylinder head and the endoscope ring. This is plausible as the measurement positions are equal in both setups. Nevertheless, there is a considerable deviation of about 40°C in the cylinder head temperature and 20°C in the mean endoscope ring temperature. These deviations are mainly a result of skip fire engine operation and the lower cooling water temperature in Setup 3. As shown, this affects the combustion behavior to a limited extent. The limited effect could be due to the recirculation of in-cylinder exhaust gas. Since the remaining residual exhaust gas acts as thermal insulation, the heat flow to the combustion chamber wall decreases to a smaller extent. The hot remaining residual exhaust gas increases heat up of the fresh charge. As a consequence, the combustion temperature is high enough to result in combustion behavior that is almost equal to that of the full-load optical engine setup running in steady state operation conditions.

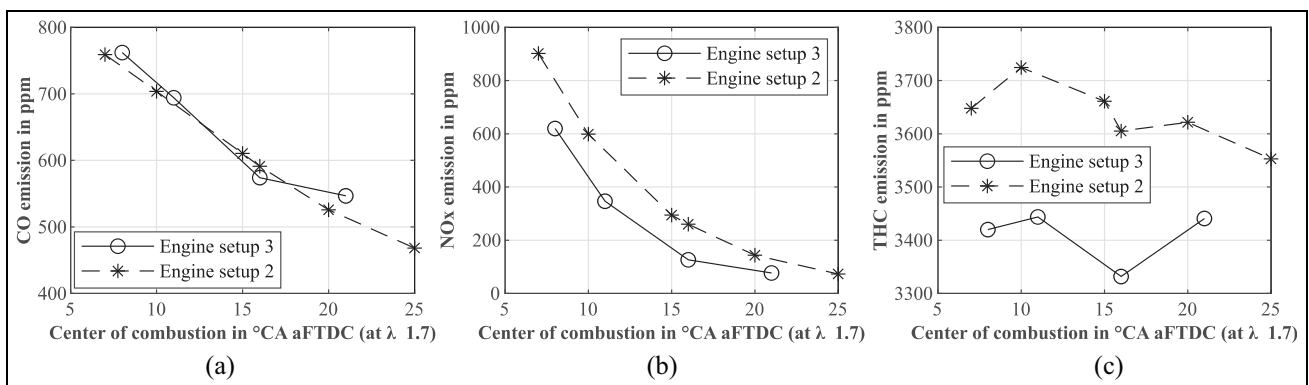


Figure 14. Emission of comparison 2: (a) CO emission, (b) NO_x emission, and (c) THC emission.

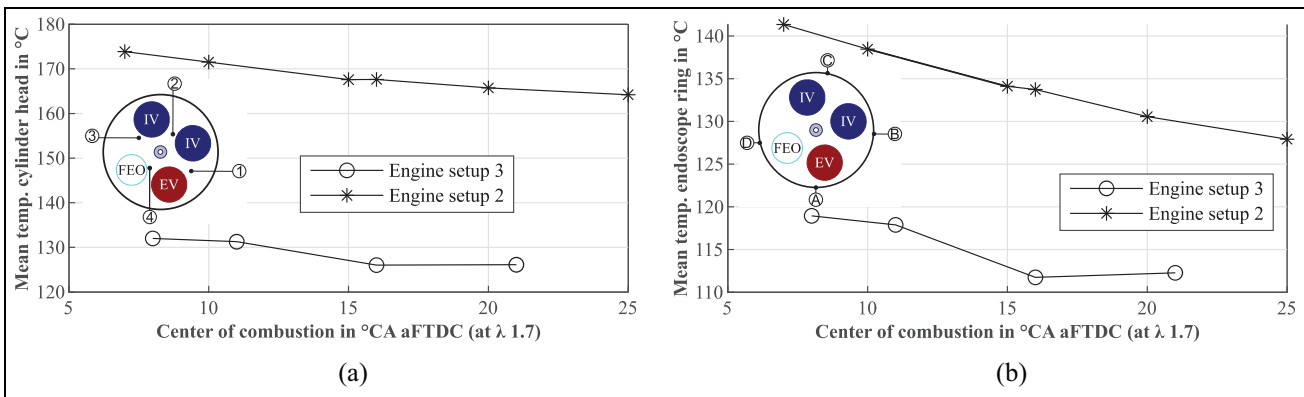


Figure 15. Wall temperature in Comparison 2: (a) mean cylinder head temperature and (b) mean cylinder wall temperature.

Summary and discussion

The aim of comparing the all-metal engine with the optical setup is to show the extent to which the two setups are comparable regarding their combustion behavior. Similar comparisons have already been made between a light duty truck engine with full optical access based on the Bowditch principle and the corresponding thermodynamic engine in Refs.^{24–26}

However, no corresponding comparison has been conducted for the larger engine size examined in this study. Yet, differences in load compatibility, wall temperatures and, in turn, emissions have been found.

The modified full-load optical engine setup (Setup 2) can attain the nominal engine load of the all-metal engine (Setup 1). Nonetheless, this Comparison 1 displays slightly different combustion behavior. This is mainly due to the slightly lower combustion temperature resulting from the cylinder wall cooling of the optical elements, which are not found in the all-metal engine. This affects the laminar burn velocity, resulting in a slightly extended burn duration, a reduced mean indicated efficiency, and higher CO and THC emissions. Although the combustion behavior shows slightly different behavior, the differences between Setup 2 and Setup 1 are relatively small:

- 10% for the burn duration (MFB10-90)
- 1% for the indicated mean efficiency, and
- 0.5% for CoV_{IMEP}

In contrast, the THC emissions in the optical setup differ by almost 50%. Nevertheless, both setups display the same qualitative behavior and tendencies in the air-fuel equivalence ratio variations. Therefore, the investigations of the full-load optical engine setup are comparable with those conducted on the all-metal engine if one considers offset in the values. To determine if those offsets are constant throughout all operation points further investigations have to be carried out based on the test setups of comparison 1. If linearity between Setup 1 and 2 can be ascertained, a scaling model approach could be derived to transfer the findings of the optical full-load engine to the all-

metal engine. In addition, further design modifications can be applied to reduce the additional dead volume of Setup 2 for better comparability of the engine-out emissions.

Similarly, the difference between the full-load optical engine setup (Setup 2) and the full optical one (Setup 3) is quite small in terms of the heat release rate and combustion pressure trace. Although the adapted operation strategy of the full optical engine results in lower wall temperatures in the cylinder head and endoscope ring, it only affects the combustion behavior to a limited extent. The fueling of the engine as well as the air mass flow are stable during the measurement time resulting in reliable and comparable air-fuel equivalence ratios. Further, the effect of replacing the exhaust valve with the fisheye endoscope and its mount is simulated in GT-Power. The residual gas content increases by only 1.1% compared to the full-load optical engine.

Concerning the engine-out emissions the skip fire operation strategy has the highest impact on the NO_x emissions as their occurrence proves very unstable during the measurement duration. This is especially due to the combustion process where cyclic variation have a great influence on the maximum combustion temperature and therefore on NO_x formation. The THC and CO emissions on the other hand show a reliable behavior. Nevertheless, all investigated emission tendencies seem reasonable and can be explained by known factors.

All in all, despite some minor differences both optically accessible engines show a comparable behavior.

Comparing the full optical setup with the all-metal engine in an indirect comparison, a significant deviation in the cylinder wall temperature can be determined due to the adapted skip fire engine operation strategy, the reduced coolant temperature, and the enhanced cooling concept. Further, an altered amount of engine-out emissions between both setups have to be expected, but they also show comparable and predictable tendencies in emission formation. This is especially due to the more realistic thermodynamic behavior of the new full optical engine design which at least offers a longer fired operation time than a design according to Bowditch with only 70 fired cycles (cf. Gleis et al.¹³).

As for both optical setups the nominal engine speed has to be slowed by half to prevent the camera from damage, the transferability of the results have to be considered. As the engine speed directly affects the timescale, the mixture preparation and combustion are altered. This results in altered burn duration, emission formation and engine efficiency. The causes of the effects produced at a different engine speed are nevertheless transferable, as the timescale effect is also considered, and the results are evaluated with respect to this. All in all, the investigations display good comparability of the engine setups and hint at reliable quantifiable offsets.

Conclusion and outlook

The reliability of the optical designs is validated by experimental investigations to evaluate the comparability of the all-metal engine to the full-load optical setup as well as in an intermediate step a comparison of the setups to the full optical engine. The findings present the differences in engine behavior due to the modifications and adaptation of the engine's operating conditions. The results demonstrate good comparability in terms of combustion behavior. However, there is a discernible difference in the engine-out emissions. The insights obtained render further investigations feasible, the results of which can be evaluated and transferred to the behavior of the all-metal engine. Eicheldinger et al.,³⁴ for example, references the usability of the full-load optical engine design investigating abnormal combustion of the engine fueled with hydrogen. To improve the performance of the fish-eye setup, water cooling of the fisheye endoscope could increase the load and measurement time until full steady-state engine operation is reached, resulting in increased comparability, particularly since the combustion stability and the NO_x stability would increase.

Further investigations based on fisheye endoscopic access will be carried out in due course to gain an understanding of the use of in-cylinder combustion to push renewable fuels beyond existing limits.

Author contributions

The entire writing, implementation, evaluation and interpretation of the depicted experimental data and the design of the optical test engine belong to S. Karmann. S. Eicheldinger supported the experiments at the test rig. The remaining co-authors supported the work with their reviews.

Declaration of conflicting interests





The author(s) declared no potential conflicts of interest with respect to the research, authorship, and/or publication of this article.

Funding

The author(s) disclosed receipt of the following financial support for the research, authorship, and/or publication of this

article: This work received funding from the German Federal Ministry for Economic Affairs and Energy under the funding code 03EIV013B.

ORCID iDs

Stephan Karmann  <https://orcid.org/0000-0002-0920-7222>
 Stefan Eicheldinger  <https://orcid.org/0000-0003-1211-1157>
 Maximilian Prager  <https://orcid.org/0000-0003-2507-6530>
 Malte Jaensch  <https://orcid.org/0000-0003-0550-1421>

References

1. Pressemitteilung Eurostat. Erneuerbare Energien in der EU im Jahr 2018: Eurostat, <https://ec.europa.eu/eurostat/documents/2995521/10335442/8-23012020-AP-DE.pdf/ab13eb1f-fe9d-9a57-44b3-98f0011e8697> (2020, accessed 9 September 2021)
2. Hultqvist A, Christensen M, Johansson B, Richter M, Nygren J, Hult J, et al. The HCCI combustion process in a single cycle – speed fuel tracer LIF and chemiluminescence imaging. SAE technical paper 2002-01-0424, 2002.
3. Einecke S, Schulz C and Sick V. Measurement of temperature, fuel concentration and equivalence ratio fields using tracer LIF in IC engine combustion. *Appl Phys B* 2000; 71(5): 717–723.
4. Pöllmann S, Härtl M and Wachtmeister G. Injection process of the synthetic fuel oxymethylene ether: optical analysis in a heavy-duty engine. SAE technical paper 2020-01-2144, 2020.
5. Fatouraie M and Wooldridge M. Optical investigation of the effects of ethanol/gasoline blends on spark-assisted HCCI. *J Eng Gas Turbines Power* 2014; 136(8).
6. Lee C-f, Pang Y, Wu H, Hernández JJ, Zhang S and Liu F. The optical investigation of hydrogen enrichment effects on combustion and soot emission characteristics of CNG/diesel dual-fuel engine. *Fuel* 2020; 280: 118639.
7. Chen L, Wei H, Zhang R, Pan J, Zhou L and Feng D. Effects of spark plug type and ignition energy on combustion performance in an optical SI engine fueled with methane. *Appl Therm Eng* 2019; 148: 188–195.
8. Peñaranda A, Martinez Boggio SD, Lacava PT, Merola S and Irimescu A. Characterization of flame front propagation during early and late combustion for methane-hydrogen fueling of an optically accessible SI engine. *Int J Hydrogen Energy* 2018; 43(52): 23538–23557.
9. Jakob M. *Optical investigation of diesel-engine related combustion processes*. Dissertation, Aachen: Rheinisch-Westfälische Technische Hochschule, Germany, 2014.
10. Greis EA. *Laseroptische Untersuchungen des Verbrennungsprozesses in einem PKW-Dieselmotor*. Dissertation, Aachen: Rheinisch-Westfälische Technische Hochschule, Germany, 2007.
11. Bensing D. *Aufbau eines optisch zugänglichen Einzylinder-Viertaktmotors und charakterisierende Messungen*. Dissertation, Universität Duisburg-Essen, Duisburg, Germany, 2013.
12. Unfug F. Experimentelle und numerische Untersuchung der Verbrennung eines mittelschnelllaufenden 4-Takt Dieselmotors. Dissertation, Berlin: Logos Berlin, Germany, 2013.
13. Gleis S, Frankl S, Prager M and Wachtmeister G. Optical analysis of the combustion of potential future E-Fuels with a high pressure dual fuel injection system. In: *14. internationales AVL powertrain diagnostik symposium*, Baden-Baden, Germany, 2020.

14. Hult J and Mayer S. A methodology for laser diagnostics in large-bore marine two-stroke diesel engines. *Meas Sci Technol* 2013; 24(4): 45204.
15. Wellander R, Rosell J, Richter M, Alden M, Andersson O, Johansson B, et al. Study of the early flame development in a spark-ignited lean burn four-stroke large bore gas engine by fuel tracer PLIF. *SAE Int J Engines* 2014; 7(2): 928–936.
16. Duong J. *Combustion visualization in a large bore gas engine*. Thesis, Lund: Lund University, 2013.
17. Disch C and Waldenmaier U. *High-speed flame chemiluminescence investigations of prechamber jets in a lean mixture large-bore natural gas engine*, 27th CIMAC World Congress, Shanghai, China, 13–16 May 2013, Paper-No.: 79/1-16.
18. Tsekenis SA, Wilson D, Lengden M, Hyvönen J, Leinonen J, Shah A, et al. Towards in-cylinder chemical species tomography on large-bore IC engines with pre-chamber. *Flow Meas Instrum* 2017; 53: 116–125.
19. Korb B, Kuppa K, Nguyen HD, Dinkelacker F and Wachtmeister G. Experimental and numerical investigations of charge motion and combustion in lean-burn natural gas engines. *Combust Flame* 2020; 212: 309–322.
20. Karmann S, Prager M and Wachtmeister G. Conceptual investigations on full optical accessibility to large-bore medium-speed engines. *SAE Int J Engines* 2019; 12(3): 291–308.
21. Bowditch FW. A new tool for combustion research a quartz piston engine. SAE technical paper 610002, 1961.
22. Korb B and Gleis S. Auslegung und Entwicklung eines volloptischen Einzylinder-Großmotors mittels Ansys Workbench und einer vereinfachten FKM-Richtlinie. In: *Conference proceedings | Die Fachkonferenz zur Numerischen Simulation*. Grafing bei München, Darmstadt: CADFEM GmbH, 2015.
23. Gleis S, Frankl S, Waligorski D, Prager M and Wachtmeister G. Investigation of the High-Pressure-Dual-Fuel (HPDF) combustion process of natural gas on a fully optically accessible research engine. In: *2019 JSAE/SAE powertrains, fuels and lubricants international meeting*, Kyoto, Japan, 2019.
24. Colban WF, Kim D, Miles PC, Oh S, Opat R, Krieger R, et al. A detailed comparison of emissions and combustion performance between optical and metal single-cylinder diesel engines at low temperature combustion conditions. *SAE Int J Fuels Lubr* 2009; 1(1): 505–519.
25. Kashdan J and Thirouard B. Optical engines as representative tools in the development of new combustion engine concepts. *Oil Gas Sci Technol Rev IFP Energies Nouvelles* 2011; 66(5): 759–777.
26. Kashdan JT and Thirouard B. A comparison of combustion and emissions behaviour in optical and metal single-cylinder diesel engines. *SAE Int J Engines* 2009; 2(1): 1857–1872.
27. Karmann S, Friedrich C, Prager M and Wachtmeister G. Realization of a fully optically accessible medium speed large bore engine using a fisheye optic. In: *ASME 2020 power conference*, 4–5 August 2020. New York: ASME.
28. Eicheldinger S, Bartkowski T, Schröder A, Prager M and Wachtmeister G. Experimental investigation on the influence of brake mean effective pressures up to 30 bar on the behavior of a large bore otto gas engine. SAE technical paper 2019-01-2224, 2019.
29. Karmann S, Klier B, Röhrle H, Prager M and Wachtmeister G. Design of an endoscopic fully optically accessible high speed large bore engine. *Int J Engine Res* 2021; 15(6)
30. Frankl S, Gleis S and Wachtmeister G. Interpretation of ignition and combustion in a full-optical high-pressure-dual-fuel (HPDF) engine using 3D-CFD methods. In: *CIMAC CONGRESS 19, 29th CIMAC world congress on combustion engine, meeting the future of combustion engines*, Vancouver, BC, CA, 10–14 June 2019.
31. Weber S, Stegmann R, Prager M and Wachtmeister G. The effect of inlet valve timing and engine speed on dual fuel NG-diesel combustion in a large bore engine. *SAE Int J Engines* 2018; 11(2): 229–246.
32. Korb B, Prager M, Wachtmeister G, Kuppa K and Dinkelacker F. Ursachen und Reduzierung der CH₄-Emissionen in Biogasmotoren; Teilvorhaben 1. Fachagentur Nachwachsende Rohstoffe e.V. (FNR), [## Appendix](https://www.tib.eu/de/suchen?tx_tibsearch_search%5Baction%5D=do_wnload&tx_tibsearch_search%5Bcontroller%5D=Download&tx_tibsearch_search%5Bdocid%5D=TIB_KAT%3A871460009&cHash=d7b46a65f628785a07a6541ca4302f28#download-mark(2016, accessed 2016 July 29).
33. Karmann S, Kunkel C, Prager M and Wachtmeister G. A new optical access for medium speed large bore marine engines under full-load operating conditions. <i>SAE Int J Engines</i> 2021; 14(6): 867–883.
34. Eicheldinger S, Karmann S, Prager M and Wachtmeister G. Optical screening investigations of backfire in a large bore medium speed hydrogen engine. <i>Int J Engine Res</i>. Epub ahead of print 20 October 2021. DOI: 10.1177/14680874211053171.
35. Karmann S, Eicheldinger S, Prager M and Wachtmeister G. Optical and thermodynamic investigations of a methane and hydrogen blend fueled large bore engine. <i>Int J Engine Res</i>. Epub ahead of print 3 January 2022. DOI: 10.1177/14680874211066735.
36. Park C, Kim C, Choi Y, Won S and Moriyoshi Y. The influences of hydrogen on the performance and emission characteristics of a heavy duty natural gas engine. <i>Int J Hydrogen Energy</i> 2011; 36(5): 3739–3745.
37. Kuppa K, Nguyen HD, Goldmann A, Korb B, Wachtmeister G and Dinkelacker F. Numerical modelling of unburned hydrocarbon emissions in gas engines with varied fuels. <i>Fuel</i> 2019; 254: 115532.

</div>
<div data-bbox=)

Notation

AHRR	Apparent heat release rate
CoC	Center of combustion \triangle MFB 50
CHT	Conjugate heat transfer
FEO	Fisheye optic
FOV	Field of view
MFB	Mass fraction burned
FTDC	Firing top dead center
aFTDC	After firing top dead center
bFTDC	Before firing top dead center
EVO	Exhaust valve open
EVC	Exhaust valve close
IVO	Inlet valve open
IVC	Inlet valve close
OME	Oxymethylenether